Nanoscale

ROYAL SOCIETY OF CHEMISTRY

PAPER

View Article Online
View Journal | View Issue

Cite this: *Nanoscale*, 2025, **17**, 28165

Lattice dynamics of layered kagome lattice material Nb_3Br_8 investigated *via* Raman spectroscopy and DFT

Dylan A. Jeff,†[a,b] Ravinder Sharma,†[a,b] Gabriel Marciaga,[a,b] Favian Gonzalez,[a,b] Kamal Harrison,[a,b] Yuzhou Zhao,[c,d] Tharindu Fernando,[d] Madhab Neupane,[a] Jihui Yang,[c] Jiun-Haw Chu,[d] Xiaodong Xu,[c,d] Ting Cao[c] and Saiful I. Khondaker*[a,b]

In this paper, the lattice dynamics of bulk and few layer Nb_3Br_8 flakes are investigated *via* linearly polarized Raman spectroscopy and density-functional theory (DFT) to study the crystal's phonon modes and their symmetrical representations. 18 phonon modes are resolved in exfoliated bulk, 10 of which are E_g modes and 8 are A_{1g} modes, in close agreement with results obtained from DFT analysis. A near-resonant condition is revealed by excitation-dependent Raman experiments conducted with wavelengths between 473 nm–785 nm when a 532 nm source is used. It is shown *via* layer-dependent studies that the intensity of bands in the Raman spectra decrease and a slight shift in frequency is experienced in thin layers, however their symmetries remain consistent with bulk. Finally, no changes in Raman selection rules for the phonon modes are observed in a polarized Raman study conducted above the structural phase transition temperature of 387 K, suggesting their insensitivity to the phase transition. This study serves to establish a foundation for future studies of Nb_3Br_8 and its characteristic Raman-active phonon modes across different structural phases and thicknesses down to bilayer.

Received 6th August 2025,
Accepted 24th November 2025

DOI: 10.1039/d5nr03318g

rsc.li/nanoscale

1. Introduction

Niobium bromide (Nb_3Br_8) is a member of the niobium halide (Nb_3X_8, X = Cl, Br, I) family of layered van der Waals materials which have recently gained significant interest due to their potential as platforms for studying exotic electronic and magnetic properties, their exceptional visible and infrared light absorption capabilities, and their possible applications in a new generation of electronic, spintronic, and optoelectronic devices.[1–5] These materials crystallize in a breathing kagome lattice featuring niobium trimers oriented as corner sharing triangles with alternating bond lengths resulting in the "breathing" structure.[6] Due to intrinsic electron localizations induced by the kagome lattice, the Nb_3X_8 family are prime candidates for the study of electron correlation effects, demonstrated by the presence of topologically flat and weakly dispersing bands in bulk which were resolved *via* angle-resolved photoemission spectroscopy (ARPES).[7–9] The ARPES measurements reveal a semiconducting band gap in the bulk crystals, while first-principles calculations on the monolayer systems suggest the presence of a Mott insulating electronic state.[10–12] Additionally, due to the unique breathing nature of the Nb_3X_8 kagome structure, their monolayers are expected to exhibit intrinsic multiferroicity *via* the spontaneous formation of dipoles, providing a platform for ferroelectricity, ferromagnetism, and ferrovalley to coexist.[13,14] Recent experimental and theoretical studies indicate the promise in thinning Nb_3X_8 crystals down to the 2D limit thanks to their favorable interlayer cleavage energies for mechanical exfoliation.[15,16] In fact, Nb_3Br_8 has been utilized as a constituent layer in a field-free Josephson diode heterostructure where, together with $NbSe_2$, the heterostructure breaks inversion symmetry and forms a superconducting state without the need of an external magnetic field.[17]

Nb_3Br_8 crystallizes as a trigonal system with point group D_{3d} and rhombohedral space group $R\bar{3}m$ (no. 166).[18] This crystal also been shown to undergo a simultaneous structural and magnetic phase transition, from a low temperature non-magnetic β-phase consisting of 6 layers per unit cell to a high

---

[a] Department of Physics, University of Central Florida, Orlando, FL 32816, USA. E-mail: saiful@ucf.edu
[b] NanoScience Technology Center, University of Central Florida, Orlando, FL 32826, USA
[c] Department of Materials Science and Engineering, University of Washington, Seattle, WA 98195, USA
[d] Department of Physics, University of Washington, Seattle, WA 98195, USA

† These authors contributed equally to this work.

temperature paramagnetic α-phase consisting of 2 layers per unit cell due to a temperature induced change in stacking order.[19–21] The transition temperature is reported as 382 K during cooling cycle and 387 K during heating cycle.[19] Despite being an interesting material and promising candidate for the study of exotic 2D electronic and magnetic properties, investigations of the lattice dynamics of Nb_3Br_8, such as the number and frequencies of the Raman-active phonon modes and their respective symmetries, atomic displacements, thickness dependence, and the effect of the temperature induced phase transitions on the phonon modes remains elusive. As crystals capable of hosting exotic electronic and magnetic properties because of their natural geometries, further research focused on characterizing and comparing these physical properties are of key interest. These studies serve as significant advances in our fundamental understanding of layered Nb_3Br_8 and other members of the niobium halide family materials for future studies and applications.

In this work, we study the lattice dynamics of exfoliated bulk and few-layer Nb_3Br_8 flakes *via* linearly polarized Raman spectroscopy. The crystals were synthesized *via* chemical vapor transport (CVT) and exfoliated onto silicon substrates using the scotch-tape method. Raman measurements at different excitations (473–785 nm) reveal that the best peak resolution occurs when using a 532 nm excitation source, suggesting a near-resonance effect between the laser's energy and the energy of an electronic transition in the material. By varying the angle between polarization of the incident light with respect to the polarization of the scattered light, we resolved the symmetries of 18 different Raman active phonon modes in a bulk sample. Of those 18, 8 were found to be A_{1g} symmetric and 10 to be E_g symmetric. These findings are supported by the calculated frequencies and symmetrical representations from our first principles density functional theory (DFT) analysis. From the DFT results, we also analyzed the atomic displacements of these phonon modes. Furthermore, layer-dependent studies show decreasing Raman peak intensity and slightly shifted peak frequencies with decreasing layer thickness. Further polarization dependent studies on a 2L sample show no change in phonon symmetry, demonstrating an unchanged $R\bar{3}m$ crystal phase down to 2L. Linearly polarized Raman measurements at 443 K show no changes in the selection rules for the Raman active phonon modes, indicating that the structural phase transition from low temperature β-phase to high temperature α-phase of Nb_3Br_8 does not result in a transition to a different space group. This work serves to establish a rich understanding of Nb_3Br_8's characteristic lattice dynamics and crystal structure under varying conditions *via* Raman scattering.

2. Methods

Crystal growth and characterization

The Nb_3Br_8 single crystal was synthesized using a chemical vapor transport method.[9,19] 0.1084 g of highly purified Nb powder (99.99%, 325 mesh from Alfa Aesar) and 0.6564 g of $NbBr_5$ (99.9% from Strem Chemicals Inc.) were placed into a quartz tube (12.75 mm OD × 10.5 mm ID × 12 cm) and sealed under a vacuum of <20 mTorr. The sealed tube was then loaded into a two-zone furnace, where both heating zones were first ramped to 200 °C for an hour and held constant for a dwell time of 4 hours. The heating zones were then ramped over the course of 10 hours to reach temperatures of 830 °C on the precursor side and 785 °C on the growth side. The dwell time for this growth period was 6 days. Following the growth period, the crystals were naturally cooled down for 8 hours, where the precursor side was cooled down to 20 °C and the growth side was cooled down to 350 °C, dwelling for 3 hours. This resulted in the synthesis of optically flat and shiny crystals. The crystal structure was characterized *via* single crystal X-ray diffraction (SCXRD) using a diffractometer (Rigaku MiniFlex 600) with a Cu Kα radiation source of wavelength λ = 1.5418 Å. The samples were placed on a zero-background silicon sample holder and the data was collected in the 2θ range of 10° to 90°, with a step size of 0.02° and a counting time of 10 seconds per step.

The magnetic susceptibility (χ) of the grown crystal was measured using a physical property measurement system (Quantum Design PPMS DynaCool). Bulk Nb_3Br_8 samples were varnished onto a non-magnetic quartz paddle sample holder using GE-7031 varnish. Background subtractions were performed using the same sample holder with only the varnish as the background source. Once mounted, measurements were performed in steps of 1 K between the temperatures of 2 and 400 K. The magnetic moment was measured as the magnetic field was swept from −5 to 5 T at each temperature. The magnetic susceptibility of the sample at each temperature step was then extracted by fitting the slope of the magnetic moment between −5 and 5 T.

Mechanical exfoliation of Nb_3Br_8

Nb_3Br_8 flakes were mechanically exfoliated using Nitto tape directly from bulk crystal onto a Si wafer with a 250 nm SiO_2 capping layer. Optimal exfoliated flakes were then selected for further analysis by comparing their color contrast and transparency under an optical microscope. Atomic force microscopy (AFM) study was conducted using a SmartSPM1000 scanning probe microscope and a Park Systems NX10 under ambient conditions and in non-contact mode to determine the thickness and layer number of the exfoliated flakes.

Raman spectroscopy

Raman spectroscopy measurements were performed using a LabRAM HR Evolution confocal Raman microscope (Horiba Scientific) in backscattering geometry under ambient conditions. An 1800 gr mm^{-1} grating was used to collect and disperse the Raman signal. The linearly polarized, layer-dependent, and high temperature Raman measurements were taken using a 532 nm laser with a ultra-low frequency filter focused *via* a 100× objective lens (NA = 0.9, WD = 0.21 mm), resulting in a laser spot size of about 1 μm. The polarization dependent experiments were performed by introducing a half-wave plate, an analyzer, and a scrambler in the optical path of the Raman system. The half-wave plate is placed in the path of incidence, with which we vary the polarization of the incident light. The scattered light is then passed through an analyzer placed in between the sample and the detector, where it is linearly polarized and then passed through a scrambler to improve the efficiency of the grating. Excitation-dependent Raman spectroscopy performed with excitation wavelengths of 473, 532, 633, and 785 nm was conducted to investigate the resonant Raman effect of Nb_3Br_8. In our analysis we fit each Raman spectrum with a Gaussian–Lorentzian function to determine the frequencies and intensities of the Raman modes, which are then averaged over multiple accumulations. The spectral resolution of our system was 0.1 cm^{-1} which was determined from the standard deviation of fitting the peak at 520.7 cm^{-1} of 20 different spectra collected from a clean silicon substrate. The polar plot fittings of our experimental data were performed in OriginPro using a nonlinear fit with eqn (2) and (3) defined in the discussion section of the manuscript.

Computational methods

A density functional theory approach was implemented to perform first-principles calculations in the Quantum ESPRESSO package version 6.4.1.[22] Scalar-relativistic Optimized Norm-Conserving Vanderbilt Pseudopotential (ONCVPSP)[23,24] were used together with the Perdew–Burke–Ernzerhof generalized gradient approximation.[25,26] Long-range dispersive interactions were included *via* the Grimme D2 van der Waals correction.[27]

For the plane-wave basis, a kinetic energy cutoff of 95 Ry was employed for the electronic wavefunctions, while the charge density cutoff is determined self-consistently within the norm-conserving formalism. Structural relaxations were carried out with a convergence threshold for total energy of 10^{-8} Ry and a maximum of 200 electronic iterations allowed per step, with an enhanced charge-density mixing factor (corresponding to an "upscale" factor of 100 in QE) to improve convergence. Atomic forces were minimized until they were below 10^{-3} Ry $Bohr^{-1}$. The Brillouin zone was sampled with a 10 × 10 × 3 Monkhorst–Pack *k*-point mesh, and a Gaussian smearing of 0.007 Ry was applied to aid convergence. K-point mesh convergence tests showed that the total energy became effectively constant beyond an 8 × 8 × 3 grid, with no meaningful gain in accuracy at higher densities, supporting our use of a 10 × 10 × 3 mesh in our calculations. A Hubbard potential of $U = 1$ eV was used on niobium d orbitals to account for on-site interactions.[28]

Phonon frequencies and eigenvectors were calculated using density functional perturbation theory (DFPT) at the Γ point. The phonon calculations were carried out on the nonmagnetic structure relaxed with $U = 1$ eV for consistency, and the same U value was included in the perturbative calculations. Tests with interlayer antiferromagnetic ordering showed only minor changes (≈0.3 meV, or a few cm^{-1} on average) in the phonon energies, indicating that the lattice dynamics are essentially insensitive to the interlayer magnetic configuration.

3. Results and discussion

Fig. 1a & b illustrate the crystal structure of Nb_3Br_8 along the crystallographic *a*- and *c*-axis directions respectively.[29] Each layer of Nb_3Br_8 consists of a sheet of Nb atoms (gold) sandwiched between two sheets of Br atoms (blue) with van der Waals (vdW) interactions between the adjacent layers. When observing the crystal lattice from the *c*-direction (Fig. 1b), the Nb atoms in the lattice form corner sharing triangles with alternating sizes, also known as trimers, shaping the exotic breathing kagome lattice. The synthesized Nb_3Br_8 crystals were first characterized using XRD and the results are shown in Fig. 1c. The sharp peaks and minimal noise reflect the good crystallinity of the grown sample. The out-of-plane lattice parameter, *c*, was calculated *via* Bragg's law using values recorded from the peak corresponding to the 006 plane and was determined to be 38.4 Å, confirming that the grown sample is in the β-phase Nb_3Br_8 at room temperature.[6,30] Considering the six layers per unit cell in the β-phase Nb_3Br_8 lattice, we calculate the interlayer distance as approximately 6.4 Å, in close agreement with a previously reported value.[19] The magnetic moment of the grown crystal was then measured using a vibrating sample magnetometer, where the slopes of the magnetic moment (magnetic susceptibility, χ) are plotted as a function of temperature in Fig. 1d while the sample was heated. The magnetic susceptibility experiences a sharp increase in magnitude at 393 K which is in close agreement to the reported phase transition temperature of 387 K during the heating cycle.[19] This sharp increase in susceptibility is indicative of the material undergoing the expected magnetic transition from a room temperature non-magnetic phase to a high temperature paramagnetic phase accompanied with a structural phase transition from the β-phase to the α-phase.[19] The small 6 K difference observed between our experimental transition temperature and ref. 19 could be the effect of slight stoichiometric differences. The Nb_3Br_8 flakes were then mechanically exfoliated onto Si/SiO_2 substrates for further characterization. Optical images of an exfoliated bulk flake (shown in Fig. 1e) and of a 2-layer (2L) flake (shown in Fig. 1f) show the sharp contrast in transparency and color between the relatively thick and thinner counterparts. The thickness of the exfoliated bulk and 2L flakes were measured *via* AFM to be 48 nm (Fig. 1g) and 1.7 nm (Fig. 1h) respectively. Considering the interlayer distance of 0.64 nm measured *via* XRD, the expected thickness of bilayer is approximately 1.28 nm, while a trilayer would be around 1.92 nm. The measured 1.7 nm flake height on the Si/SiO_2 substrate lies in between the two theoretical values. However, it is known that AFM can overestimate the height of a 2D material due to incomplete bonding at the interface, variations in bond lengths between the material and the substrate, substrate-induced or exfoliation-induced tensile strain, and potential AFM tip adsorbates that may introduce

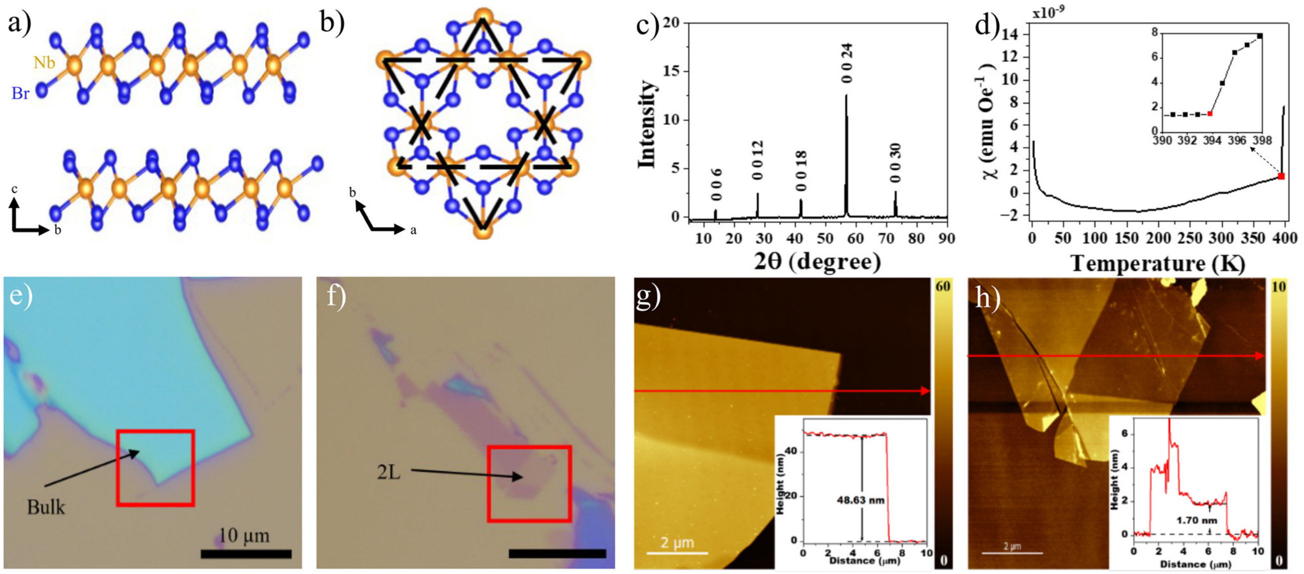

Fig. 1 Characterization of single-crystal Nb_3Br_8. (a) In-plane view of the Nb_3Br_8 lattice structure. (b) A breathing kagome lattice is formed by Nb trimers, highlighted when viewed from *c* direction. (c) Single crystal X-ray diffraction of the synthesized Nb_3Br_8 bulk crystals indicating good crystallinity and periodicity. (d) The magnetic susceptibility of Nb_3Br_8 plotted as a function of temperature showing an abrupt increase in magnetic susceptibility at 393 K shown in the inset. (e) and (f) Optical images of bulk and 2L Nb_3Br_8 exfoliations, respectively. Scale bars are 10 µm. (g) and (h) Corresponding atomic force microscopy images and height profiles (inset) of the bulk and 2L flakes respectively. The red arrows correspond to the areas from which the height profiles were taken.

measurement artifacts.[31–33] Taking these into consideration, we determine the height of the flake to correspond to that of a bilayer Nb_3Br_8.

Polarized Raman analysis

Linearly polarized Raman measurements were performed on the exfoliated Nb_3Br_8 bulk and few layer flakes using a 532 nm excitation source at room temperature to investigate the symmetries of the crystal's phonon modes and assign them to their corresponding irreducible representations. The Raman tensor, *R*, for Nb_3Br_8's point group $D3d$ (see SI Table S1) indicates that only A_{1g} or E_g symmetric phonon modes are present.[34–36] The predicted irreducible representations of the Raman-active optical phonons of Nb_3Br_8 at the Γ point of the Brillouin zone are expressed as

$$\Gamma = 8A_{1g} + 11E_g. \tag{1}$$

The polarization selection rules for each mode can be determined using the Raman intensity (I) relation, $I \propto \left|\hat{e}_i^{\dagger} \cdot R \cdot \hat{e}_s\right|^2$. Here $\hat{e}_i$ and $\hat{e}_s$ are the unit vectors associated with the polarization state of the incident and scattered light respectively. The angle between these polarization states, the polarization-angle, is given by θ. At $\theta = 0$ both the incident and scattered light are vertically polarized, therefore any changes in incident light polarization will result in equal changes to θ. In our experiments, a half-wave plate was placed in the excitation path to vary the polarization of the incident light while an analyzer was placed in the scattered path to keep the scattered light vertically polarized. Because the specific orientation of the crystalline axes are unknown in our experiment, we define ϕ as an arbitrary constant angle with respect to the *b* axis. By manipulating θ, we can study the angular dependence of intensities for each phonon mode and determine whether they are either E_g or A_{1g} symmetric.[37] In backscattering geometry (along the *c*-axis), the intensity of each Raman active mode can be expressed as:

$$I_{A_{1g}} \propto a^2 \cos^2(\theta) \tag{2}$$

$$I_{E_g} \propto I_{E_{g,1}} + I_{E_{g,2}} \propto c^2 \cos^2(\theta + 2\phi) + c^2 \sin^2(\theta + 2\phi) \tag{3}$$

where a and c are elements of R (see SI S1 for the derivations of eqn (2) and (3)). For $\theta = 90°$ (cross-polarization), $I_{A_{1g}}$ will be zero and A_{1g} modes will be "forbidden". On the other hand, E_g modes will exhibit a nonzero constant intensity regardless of the value of θ. For $\theta = 0$ (parallel polarization), both A_{1g} and E_g modes will have non-zero intensities. An excitation-dependent Raman experiment (see SI Fig. S1) was performed to discern which excitation source would be best at resolving the most modes for our linearly polarized Raman experiments, revealing that a 532 nm laser source resolves the most modes in bulk and thin layers.

Fig. 2a shows the Raman spectra of bulk Nb_3Br_8 in parallel-polarization ($\theta = 0$, red curve) and cross-polarization ($\theta = 90$, black curve) configurations.[18] Raman modes are resolved and labeled as P1–P18 on the parallel-polarized spectrum with their experimental frequencies shown in Table 1. Eqn (2) and (3) predict that all peaks are present in parallel polarization, however, we are only able to resolve 18 modes experimentally, out of the 19 predicted in eqn (1). The unobserved Raman mode will be discussed later in the theory section. Raman

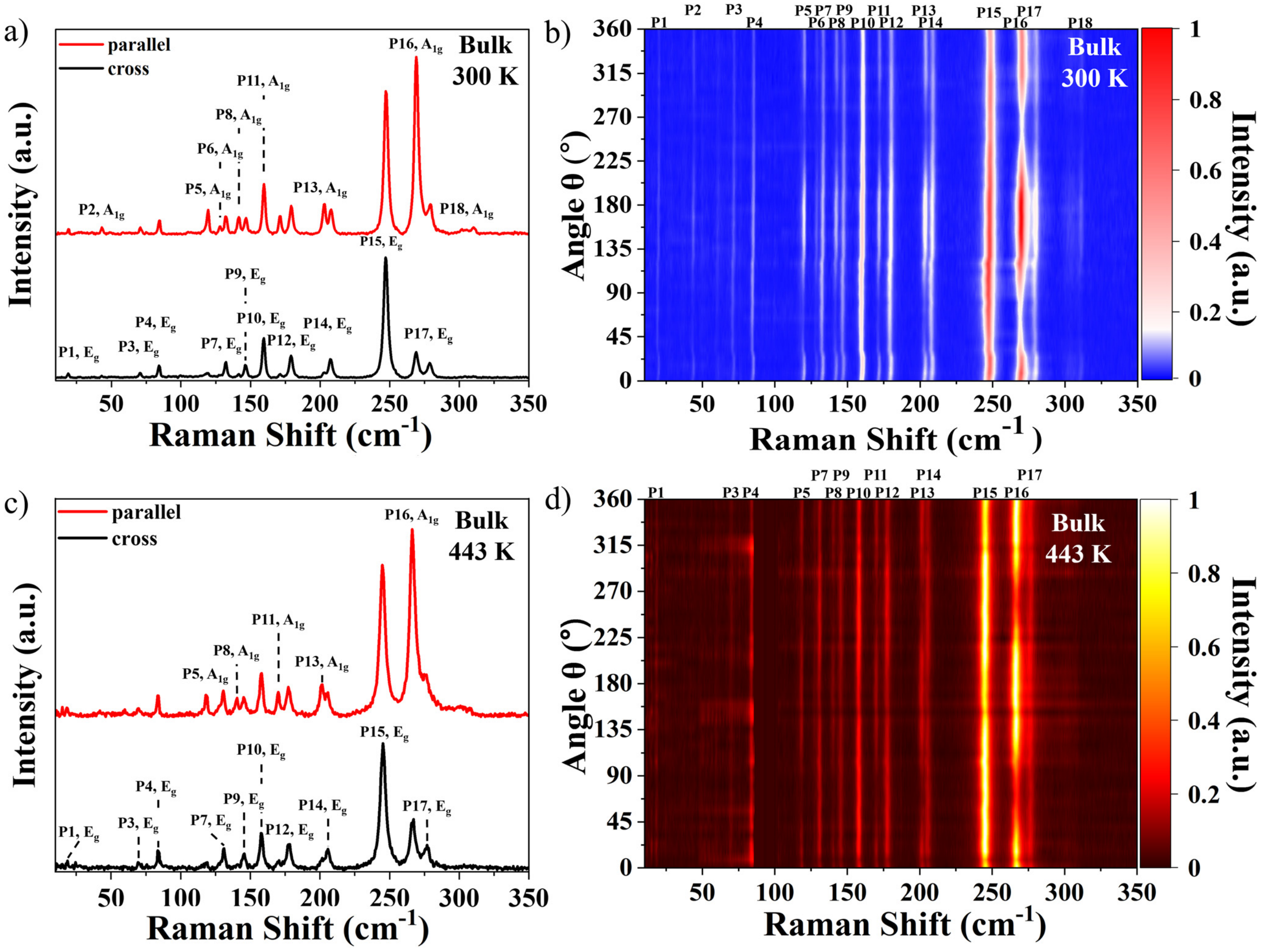

Fig. 2 Linearly polarized Raman spectra of exfoliated bulk Nb_3Br_8 flake taken with a 532 nm excitation source at room temperature and 443 K. (a) A total of 18 Raman modes were resolved in bulk at room temperature, labeled as P1–P18 in the parallel polarized spectrum (red curve), where the A_{1g} modes are labeled. A cross polarized (black curve) spectrum is plotted underneath for an insight into the polarization angle dependence of each Raman mode, where the E_g modes are labeled. (b) A color map of each phonon mode's intensity with respect to polarization angle in bulk at room temperature further reveals the polarization dependence of each Raman mode as θ is varied. (c) A total of 15 modes were resolved and labeled in the parallel bulk at 443 K. (d) A color map of phonon mode intensity with respect to polarization angle in bulk at 443 K shows the preservation of peak symmetry in the high temperature phase.

spectrum measured under cross-polarization (black curve) reveals no change in intensity for P1, P3, P4, P7, P9, P10, P12, P14, P15, and a significant reduction in intensity for P2, P5, P6, P8, P11, P13, and P16 while P18 is no longer observable. P17 also experiences a reduction in intensity in cross-polarized configurations, however this reduction is not as significant in comparison to the rest. The color map provided in Fig. 2b reveals the full θ dependence of each phonon mode in bulk Nb_3Br_8. Peaks such as P9 at 147.19 cm^{-1} that exhibit a constant intensity across all θ values are indicative of phonon modes that are polarization angle independent. In contrast, peaks like P5 at about 119.97 cm^{-1} that are most intense near θ = 0, 180, and 360 and are noticeably less intense near cross-polarized configurations such as θ = 90 and 270 are indicative of phonon modes that are polarization angle dependent. Relating these behaviors to eqn (2) and (3), we can infer that the modes which maintained a constant intensity are likely E_g symmetric while those who experienced a loss of intensity are likely A_{1g} symmetric.

The effect of the high temperature structural phase transition on the lattice dynamics of Nb_3Br_8, was studied *via* an additional linearly polarized Raman experiment on a bulk flake at 443 K. This temperature is significantly above the reported transition temperature of 387 K (ref. 19) and the transition temperature of 393 K measured in Fig. 1d. The high temperature structural phase transition occurs as the vdW stacking sequence in the lattice is rearranged. Such changes, although very slight, can have large implications on the overall electronic, magnetic, and phonon structure of the material. Although the space group symmetry of the crystal is not expected to change from the low temperature β-phase to the high temperature α-phase, as a material with many exotic

Table 1 Experimental Raman mode frequencies of bulk and 2L Nb_3Br_8 measured with a 532 nm excitation source at room temperature

	Bulk Nb_3Br	2L Nb_3Br_8	$\Delta_{\text{frequency}}$
Peak number	Frequency [cm^{-1}]	Frequency [cm^{-1}]	Frequency [cm^{-1}]
P1	19.71	—	—
P2	43.76	—	—
P3	71.41	—	—
P4	85.00	83.28	1.72
P5	119.97	118.12	1.85
P6	128.69	—	—
P7	132.92	132.04	1.69
P8	141.21	141.33	0.12
P9	147.19	146.47	0.72
P10	160.19	159.57	0.62
P11	171.74	170.72	1.02
P12	179.75	178.30	1.45
P13	203.48	202.43	1.05
P14	208.32	207.65	0.67
P15	247.94	247.24	0.7
P16	269.68	269.01	0.67
P17	279.71	278.88	0.83
P18	310.00	—	—

properties tied to its natural geometry, any modifications to that geometry can lead to a variety of unforeseen effects. Raman spectra taken at parallel and cross polarizations, and a color map of each peak's intensity with respect to the polarization angle are provided in Fig. 2c and d respectively. Compared to the 18 Raman modes we resolved in our room temperature measurements, we observe a total of 15 Raman modes at 443 K, 5 A_{1g} symmetric, and 10 E_g symmetric. Two low intensity peaks, P2 and P18, become unresolvable due to the increased thermal radiation at high temperatures generating noise that washes out the low intensity signals.[38] Additionally, a small shoulder near 127.00 cm^{-1} is observed whose frequency is close to P6 however its polarization-angle dependence could not be fitted due to its low intensity. The frequencies of each Raman mode are observed to down shift with the increase in temperature (see SI Table S2). A maximum shift of 3.44 cm^{-1} was observed for peak P16 and a minimum of 0.84 cm^{-1} for peak P8 with an average shift of 2.01 cm^{-1} from 300 K to 443 K. Because these shifts in frequency at high temperatures are small, they are likely related to the effect which the thermal expansion of the lattice has on the phonon modes of the crystal, resulting in shifts to lower values as seen in other 2D materials.[39,40] The Raman selection rules of the modes in the high temperature phase are consistent with those observed at room temperature (SI Table S2), suggesting they are insensitive to the structural phase transition.

Polar plots showing the functional dependence of each phonon mode fitted to eqn (2) or (3) are provided in Fig. 3 and SI Fig. S3 for experiments performed on bulk at 300 K and 443 K, respectively. The colored dots represent experimental data points, while the colored solid lines are fits using either eqn (2) (blue curves) or (3) (red curves). For each data point, the intensity of the peak is normalized with respect to the intensity of P15 at the corresponding angle as it is the most intense peak that does not vary with θ. Fig. 3 shows the Raman peaks P2, P5, P6, P8, P11, P13, P16, and P18 have intensities which vary with the angle of polarization, exhibiting a 2-fold symmetric response best fitted with eqn (2), confirming them as A_{1g} symmetric phonon modes (blue dots). The Raman peaks P1, P3, P4, P7, P9, P10, P12, P14, and P15 have intensities that are independent of the angle of polarization, exhibiting a circularly symmetric response and are best fitted by eqn (3), confirming their E_g symmetry (red dots). The polar plot for P17 indicates that its intensity is dependent on the value of θ, likening it to an A_{1g} peak, however considering its proximity to the relatively intense A_{1g} peak P16 as a shoulder we consider that its intensity is being influenced. To better resolve the polarization-angle dependence of this mode, a supplementary linearly polarized Raman experiment using a 473 nm wavelength excitation source was performed. Considering the broad elliptical shape of the corresponding polar plot in Fig. 3 and the circular polar plot observed in the 473 nm experiment shown in SI Fig. S2, we assign this peak as E_g symmetric. Table 2 summarizes the experimental frequencies, where we have assigned each peak their corresponding irreducible representations for bulk Nb_3Br_8 using the experimental frequencies and the polarization-angle dependencies of each mode, allowing us to differentiate between and assign modes with nearly degenerate frequencies.

Fig. 4a shows the Raman spectrum of a 2L Nb_3Br_8 flake taken at 300 K in the parallel (red curve) and cross-polarized (black curve) configurations. In parallel configuration, we observed 13 modes as opposed to the 18 modes observed in bulk. The five modes that were not observed in 2L sample are P1, P2, P3, P6, and P18 which are relatively low intensity peaks in the bulk sample. By comparing the red and black curves it is evident that P4, P7, P9, P10, P12, P14, and P15 exhibit constant intensities between both configurations and peaks P5, P8, P11, P13, P16, and P17 experience losses in intensity when the system is cross-polarized. The peak next to P18, at about 300 cm^{-1}, is attributed to a silicon peak from the substrate. A color map of intensities and frequencies as a function of θ for the 2L Nb_3Br_8 flake is provided in Fig. 4b which further corroborates our analysis of the θ independent peaks (such as P9) and the θ dependent peaks (such as P5). For a closer examination of the polarization-angle dependence of the peaks in a thin layer sample, polar plots are provided for the Raman peaks of the 2L flake (see SI Fig. S4). Due to the low intensity of the modes resolved from the 2L flake, these polar plots are more scattered but are still fitted with eqn (2) and (3). We find that all the polarization-independent E_g modes in the 2L sample remained E_g in bulk, while the polarization-dependent A_{1g} modes in 2L samples remained A_{1g} modes in bulk. The consistency of the Raman mode symmetries between the bulk and 2L structure is indicative that there are no differences in symmetry between the Raman-active phonon modes of bulk and 2L layer Nb_3Br_8.

Despite the robust phonon symmetries between bulk and thin layers, each phonon mode resolved in 2L undergoes a slight shift in frequency (shown in Table 1) and loss in inten-

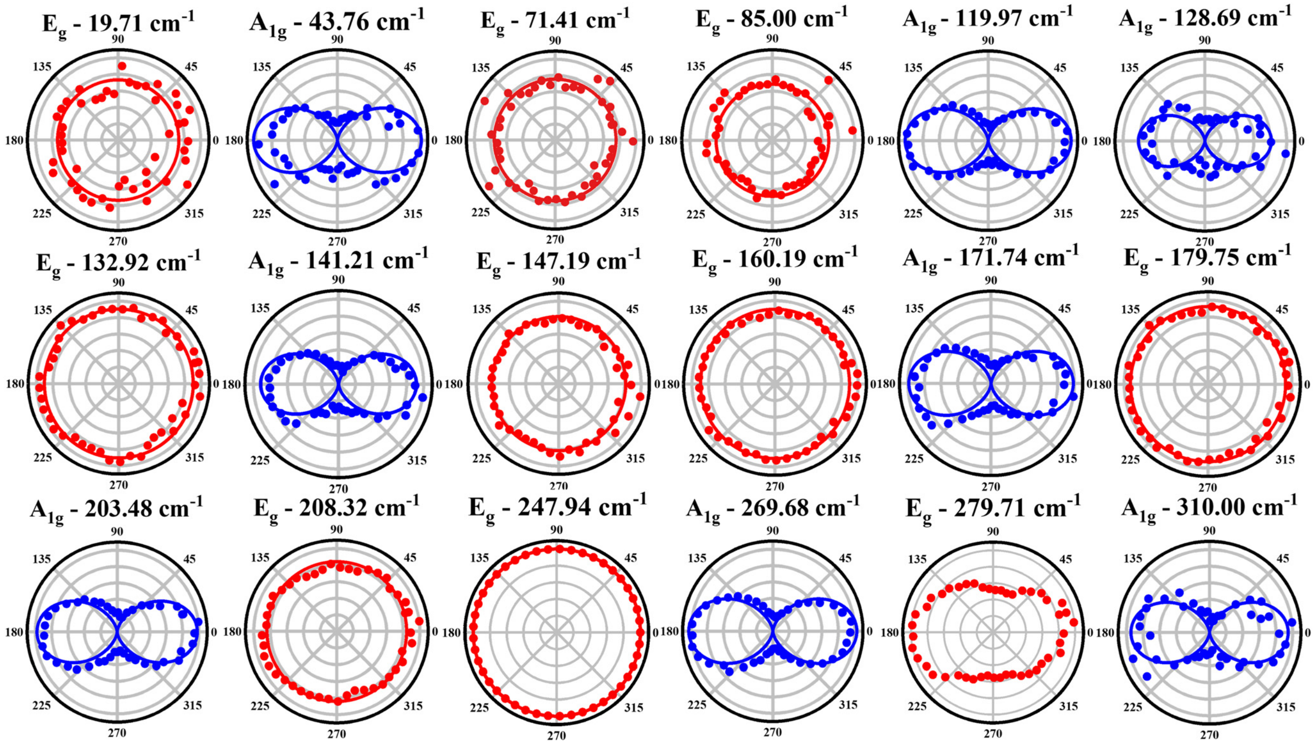

Fig. 3 Polar plots of the polarization angle dependent intensities of Nb_3Br_8's Raman active phonon modes in bulk measured with a 532 nm excitation source. E_g symmetric modes (red) exhibit intensities that are independent of the polarization angle between the incident and scattered light. A_{1g} (blue) symmetric modes exhibit polarization-dependent intensities, featuring relative maxima when the system is in parallel configuration and minima when in cross configuration. All intensities are normalized with respect to the intensity of the consistent E_g peak at 247.94 cm^{-1}.

Table 2 Calculated and experimental Raman active phonon modes of bulk Nb_3Br_8 at room temperature

Experimental		Theoretical	
Frequency [cm^{-1}]	Irreducible representation	Frequency [cm^{-1}]	Irreducible representation
19.71	E_g	17.50	E_g
43.76	A_{1g}	45.27	A_{1g}
71.41	E_g	72.31	E_g
85.00	E_g	85.90	E_g
—	—	117.68	E_g
119.97	A_{1g}	122.57	A_{1g}
132.92	E_g	128.79	E_g
128.69	A_{1g}	131.77	A_{1g}
141.21	A_{1g}	145.33	A_{1g}
147.19	E_g	150.37	E_g
160.19	E_g	155.00	E_g
171.74	A_{1g}	172.51	A_{1g}
179.75	E_g	188.51	E_g
203.48	A_{1g}	197.94	A_{1g}
208.32	E_g	198.68	E_g
247.94	E_g	239.84	E_g
269.68	A_{1g}	261.77	A_{1g}
279.71	E_g	275.50	E_g
310.00	A_{1g}	302.23	A_{1g}

sity when compared to those measured from bulk. To further visualize these shifts in frequency and losses of intensity as the flakes are thinned down, a layer-dependent analysis of the Raman modes down to thin layers was performed (see SI Fig. S5). To compare frequencies across different spectra, the peak positions of each of the Raman spectra taken at room temperature were normalized to the silicon substrate's peak at 520.7 cm^{-1}. Optical, AFM images, and height profiles of these flakes measured in this study are provided in SI Fig. S6. As shown in SI Fig. S5a, it is evident that there are slight changes in peak frequency in the thinner layers, with each mode slightly down shifting from what is observed in bulk. The layer-dependent analysis of the Raman-active modes of Nb_3Br_8 revealed a maximum shift 1.85 cm^{-1} for peak P5 and a minimum of 0.12 cm^{-1} for peak P8 with an average shift of 1 cm^{-1} between bulk and 2L. Considering the spectral resolution of our instrument is approximately 0.1 cm^{-1}, the shift observed in peak P8 is negligible while all other peaks showed non-negligible shift. The small shifts are comparable to what has been reported in several other 2D materials such as black phosphorous, which exhibits shifts in peak position between 1–3 cm^{-1} from bulk to 4L,[41] and Nb_3Cl_8, where the shift observed from bulk to a 6L flake was between 1.2–2.1 cm^{-1}.[16] Furthermore, in $Ta_2Pd_3Te_5$ no thickness-dependent shift in peak frequency were observed.[42] The Raman peak intensities show more drastic changes with intensities decreasing with layers number (see SI Fig. S5b). The intensities show a maximum decrease of 60.6% for peak P8 and a minimum of 34.0% for peak P4 with an average of about 45.6% from bulk

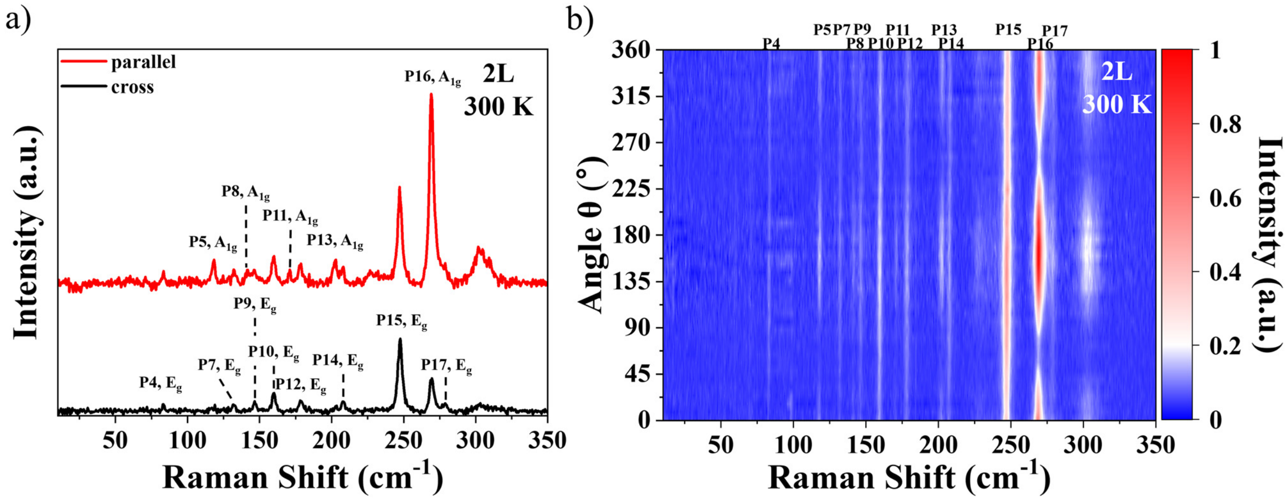

Fig. 4 Linearly polarized Raman spectra of an exfoliated 2L Nb_3Br_8 flake taken with a 532 nm excitation source at room temperature. (a) The Raman spectra of 2L Nb_3Br_8 under parallel (red curve) and cross polarized (black curve) configurations indicate similar peak polarization dependence compared to what is seen in bulk. (b) A color map of each phonon mode's intensity with respect to polarization angle in 2L Nb_3Br_8 is provided to show the full θ dependence of each mode in thin layers.

down to thin layers. The peak intensities *vs.* layer number for each peak can be fitted reasonably well with straight lines with non-zero intercepts (see SI Table S3). The observed shifts in frequency and losses of intensity are likely due to the changes in the interlayer coupling of the material and the effects of dielectric screening present as the as the vdW material approaches the 2D limit.[43]

Density functional theory analysis

For comparison with our experimental studies, DFT calculation was used to obtain the frequencies of each Raman active phonon mode in bulk Nb_3Br_8 (Table 2) and their associated atomic displacements (Fig. 5); which was then analyzed to determine the irreducible representations of each mode (Table 2). The experimental and relaxed lattice parameters utilized in our calculation are summarized in Table 3. We used the experimental hexagonal lattice parameters reported in ref. 6: a = 7.080 Å, c = 38.975 Å, γ = 120°. For the quantum ESPRESSO calculations, these parameters were expressed in a convenient reduced oblique form using the following lattice vectors: $a1$ = (3.54000, 2.04382, 12.99167); $a2$ = (−3.54000, 2.04382, 12.99167); $a3$ = (0.00000, −4.08764, 12.99167). The geometry of the material is unchanged as the vectors describe the same lattice in the basal plane. Since the effective in-plane constant becomes $a' = a/\sqrt{3} \approx 4.08764$, the shorter oblique vectors tile the plane into the same hexagonal arrangement. Along the vertical direction, each vector carries a z-component of c' = 12.99167 Å, and together they reproduce the full experimental $c = 3 \times 12.99167 \approx 38.975$ Å. In addition, a table detailing the relaxed atomic coordinates and their corresponding Wyckoff labels is provided in SI Table S4. We note that electronic calculations were conducted for the interlayer antiferromagnetic stable ground state of the bulk material. However, the material does not have long-range magnetic order at this temperature, so to coincide with our room temperature Raman experiments, nonmagnetic calculations were used to perform phonon calculations.

Comparing the Raman mode frequencies that were calculated with those determined experimentally, it is apparent that most peaks are shifted by about 4 to 8 cm^{-1}. Despite this difference in wavenumber, the irreducible representations of each calculated peak match those determined *via* our Raman experiments. Considering these consistencies, the results of our theoretical calculations agree with the results of our experimental studies. In addition to confirming the frequencies and symmetries found in our experiments, our calculations also provided information regarding an experimentally unresolved peak near 117.68 cm^{-1} that is calculated to be E_g symmetric. The inability to resolve this peak is due to the phonon mode associated with this peak likely being a relatively low-intensity mode.

To visualize how each atom in a layer of Nb_3Br_8 is displaced due to Raman scattering, a graphical depiction of the displacements for each Raman active phonon mode were modeled and are displayed in Fig. 5. These models feature a unit cell of Nb_3Br_8, where the gold atoms represent the niobium atoms, and the blue atoms represent the Bromine atoms. Each displaced atom has a black arrow attached denoting the direction and relative magnitude of the atom's displacement when the corresponding phonon is excited. A_{1g} modes are modeled as non-degenerate, with only a single atomic displacement corresponding to each. This further confirms the nature of their response to the Raman experiment detailed within this study, where depending on the polarization of the incident light, the A_{1g} modes will be most intense when the polarization angle is in accordance with the symmetry of the A_{1g} symmetric vibrations. E_g modes on the other hand are modeled as doubly degenerate phonon modes, with two similar but orthogonal

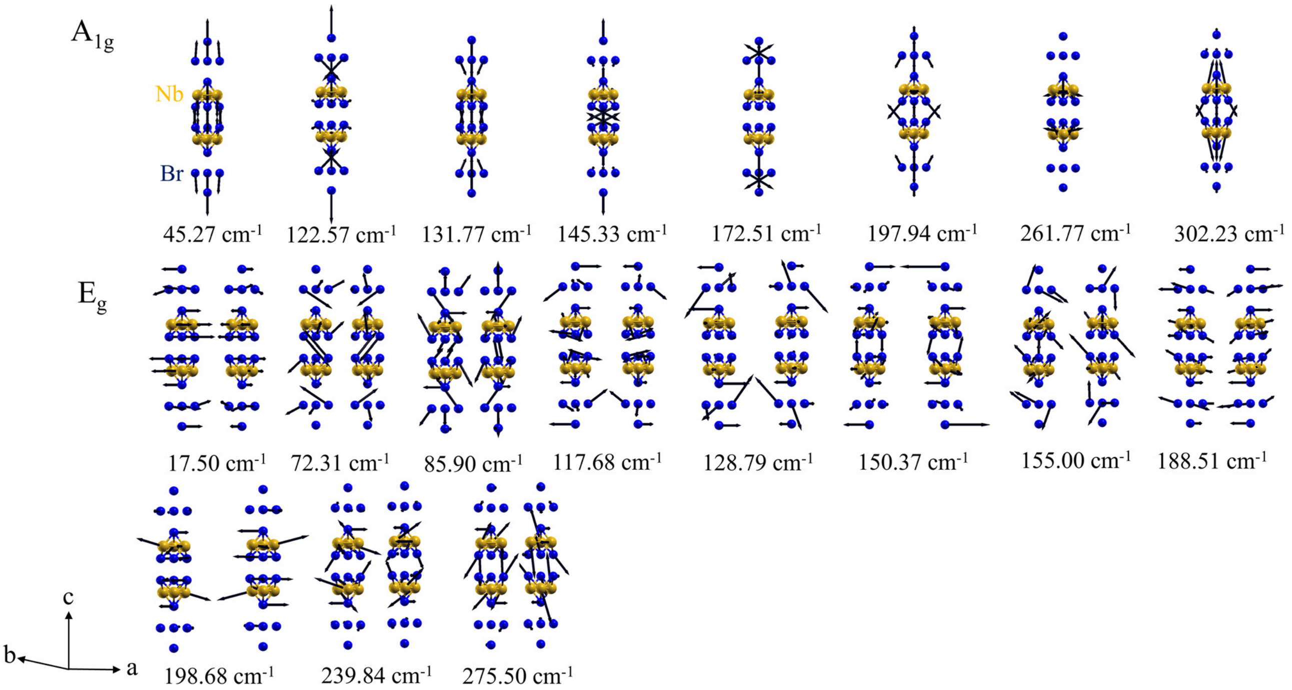

Fig. 5 Models of the atomic displacements associated with Nb_3Br_8's Raman active phonon modes obtained from the phonon eigenvectors calculated using density functional perturbation theory (DFPT). Each black arrow represents the specific displacement direction of the atom it is attached to. Gold spheres represent Nb atoms and the blue spheres represent Br atoms. The non-degenerate A_{1g} and degenerate E_g modes are grouped separately to emphasize the differences in each mode's symmetry and degeneracy.

Table 3 Experimental and relaxed lattice parameters from quantum ESPRESSO calculations

Parameter	Experimental (ref. 6)	After relaxation (QE)	Note
a	7.080 Å	7.080 Å (input)	Conventional hexagonal cell
c	38.975 Å	38.975 Å (input)	Conventional hexagonal cell
a'	—	4.0876 Å	Reduced representation ($a' = a/\sqrt{3}$)
c'	—	12.9917 Å	Reduced representation ($c' = c/3$)
Vectors	—	$a1 = (3.54000, 2.04382, 12.99167)$; $a2 = (-3.54000, 2.04382, 12.99167)$; $a3 = (0.00000, -4.08764, 12.99167)$	QE representation

atomic displacements corresponding to the same phonon mode. Due to the orthogonality of the two atomic displacements tied to the E_g modes, the Raman peaks corresponding to these phonon modes exhibit constant intensities that are independent of the polarization angle of the incident beam. These models, in conjunction with our theoretical calculation of each phonon mode's frequency, allow us to completely determine the irreducible representations of the Raman active phonon modes to study the lattice dynamics characteristic of Nb_3Br_8.

4. Conclusion

Nb_3Br_8 was synthesized *via* chemical vapor transport, characterized *via* XRD and VSM, and mechanically exfoliated down to the 2D limit. The lattice dynamics of the exfoliated Nb_3Br_8 were then investigated *via* a series of Raman and experiments and DFT calculations. We determine the symmetries and frequencies of 19 Raman active phonon modes. 18 of the 19 Raman active modes were experimentally resolved, to which we assign 10 as E_g symmetric and 8 as A_{1g} symmetric according to their response to the varying polarization configurations. The frequency and symmetry of the 19th mode was calculated *via* DFT. These experimental results and our calculations are in close agreement. The effects which excitation wavelength, layer number, and temperature-dependent crystal phase energy have on the Raman signature of Nb_3Br_8 were also studied *via* excitation-dependent, layer-dependent, and high temperature linearly polarized Raman experiments respectively. Our excitation-dependent studies indicate that using a 532 nm excitation source induces a near-resonant effect on the crystal's phonon modes, resulting in the increased resolution of the characteristic Raman spectrum of the crystal, allowing for the experimental identification of relatively low intensity peaks in both bulk and thin layers. In addition, a 473 nm laser source is found to better resolve P17 found near 279 cm^{-1}, allowing for the experimental assignment of its vibrational symmetry as E_g. Comparing the results of polarized Raman experiments performed on bulk sample and a 2L sample reveal that the crystal lattice remains in a robust crystal phase at bilayer. We also observe that as thinner flakes are isolated, the characteristic frequencies of the Raman modes of the crystal are found to slightly shift while the intensities of the Raman peaks drastically reduce with decreasing layer number. Furthermore, we show that the temperature-induced structural phase transition from β-Nb_3Br_8 to α-Nb_3Br_8 has no effect on the symmetries of Nb_3Br_8's phonon modes at 443 K, as they remain consistent in both structural phases. Finally, graphical depictions of the vibrational modes are provided to visualize the displacement of the atoms within the lattice due to Raman scattering. The results of this study are pivotal for future optical, electronic, and structural studies utilizing Nb_3Br_8 in search of novel exotic states and practical applications of the layered material.

Author contributions

Dylan A. Jeff: conceptualization, methodology, visualization, validation, formal analysis, investigation, writing – original draft, writing – review & editing. Ravinder Sharma: visualization, validation, formal analysis, investigation, writing – original draft, writing – review & editing. Gabriel Marciaga: validation, investigation, writing – original draft, writing – review & editing. Favian Gonzalez: validation, investigation. Kamal Harrison: validation, investigation. Yuzhou Zhao: validation, investigation, resources. Tharindu Fernando: formal analysis, investigation, writing – review & editing. Madhab Neupane: project administration, funding acquisition. Jihui Yang: supervision, resources. Jiun-Haw Chu: supervision, funding acquisition, resources. Xiaodong Xu: supervision, funding acquisition. Ting Cao: supervision, project administration, funding acquisition, resources. Saiful I. Khondaker: conceptualization, supervision, project administration, funding acquisition, resources, writing – review & editing.

Conflicts of interest

The authors declare no conflict of interest.

Data availability

All data that supports the findings of this study are included within the article and supplementary information (SI). Supplementary information is available. See DOI: https://doi.org/10.1039/d5nr03318g.

Acknowledgements

This work is supported by grant DMR-2121953 and DMR-2424976 from NSF Partnerships for Research and Education in Materials (PREM) at UCF.

We acknowledge the support from UW Molecular Engineering Materials Center, an NSF Materials Research Science and Engineering Center (grant no. DMR-1719797) for facilitating the DFT analysis through the use of advanced computational, storage, and networking infrastructure provided by the Hyak supercomputer system.

References

1 J. Jiang, *et al.*, Exploration of new ferromagnetic, semiconducting and biocompatible Nb(3)X(8) (X = Cl, Br or I) monolayers with considerable visible and infrared light absorption, *Nanoscale*, 2017, **9**(9), 2992–3001.
2 P. V. Pham, *et al.*, 2D Heterostructures for Ubiquitous Electronics and Optoelectronics: Principles, Opportunities, and Challenges, *Chem. Rev.*, 2022, **122**(6), 6514–6613.
3 T. Tan, *et al.*, 2D Material Optoelectronics for Information Functional Device Applications: Status and Challenges, *Adv. Sci.*, 2020, **7**(11), 2000058.
4 H. Wang, *et al.*, Two-Dimensional Ferroic Materials for Non-volatile Memory Applications, *Adv. Mater.*, 2023, e2305044.
5 M. J. Mi, *et al.*, Two-dimensional magnetic materials for spintronic devices, *Mater. Today Nano*, 2023, **24**, 100408.
6 S. N. Magonov, *et al.*, Scanning tunneling and atomic force microscopy study of layered transition metal halides Nb3X8 (X = Cl, Br, I), *J. Am. Chem. Soc.*, 2002, **115**(6), 2495–2503.
7 Z. Sun, *et al.*, Observation of Topological Flat Bands in the Kagome Semiconductor Nb(3)Cl(8), *Nano Lett.*, 2022, **22**(11), 4596–4602.
8 S. Regmi, *et al.*, Spectroscopic evidence of flat bands in breathing kagome semiconductor Nb3I8, *Commun. Mater.*, 2022, **3**, 100.
9 S. Regmi, *et al.*, Observation of flat and weakly dispersing bands in the van der Waals semiconductor Nb3Br8 with breathing kagome lattice, *Phys. Rev. B*, 2023, **108**(12), L121404.
10 S. Gao, *et al.*, Discovery of a Single-Band Mott Insulator in a van der Waals Flat-Band Compound, *Phys. Rev. X*, 2023, **13**, 041049.
11 S. Grytsiuk, *et al.*, Nb3Cl8: a prototypical layered Mott-Hubbard insulator, *npj Quantum Mater.*, 2024, **9**(8).
12 Y. Zhang, *et al.*, Mottness in two-dimensional van der Waals Nb3X8 monolayers (X=Cl, Br, and I), *Phys. Rev. B*, 2023, **107**, 035126.
13 F. Conte, D. Ninno and G. Cantele, Layer-dependent electronic and magnetic properties of Nb3I8, *Phys. Rev. Res.*, 2020, **2**, 033001.
14 Y. Feng and Q. Yang, Enabling triferroics coupling in breathing kagome lattice Nb3X8 (X = Cl, Br, I) monolayers, *J. Mater. Chem. C*, 2023, **11**(17), 5762–5769.

15 B. Mortazavi, X. Y. Zhuang and T. Rabczuk, A first-principles study on the physical properties of two-dimensional Nb3Cl8, Nb3Br8 and Nb3I8, *Appl. Phys. A: Mater. Sci. Process.*, 2022, **128**, 934.

16 D. A. Jeff, *et al.*, Raman study of layered breathing kagome lattice semiconductor Nb3Cl8, *2D Mater.*, 2023, **10**(4), 045030.

17 H. Wu, *et al.*, The field-free Josephson diode in a van der Waals heterostructure, *Nature*, 2022, **604**(7907), 653–656.

18 K. Habermehl and G. Meyer, Triniobiumoctabromide, Nb3Br8, Revisited, *Z. Naturforsch., B: J. Chem. Sci.*, 2010, **65**(6), 770–772.

19 C. M. Pasco, *et al.*, Tunable Magnetic Transition to a Singlet Ground State in a 2D van der Waals Layered Trimerized Kagome Magnet, *ACS Nano*, 2019, **13**(8), 9457–9463.

20 J. P. Sheckelton, *et al.*, Rearrangement of van der Waals stacking and formation of a singlet state at T = 90 K in a cluster magnet, *Inorg. Chem. Front.*, 2017, **4**(3), 481–490.

21 Y. Haraguchi, *et al.*, Magnetic-Nonmagnetic Phase Transition with Interlayer Charge Disproportionation of Nb (3) Trimers in the Cluster Compound Nb(3)Cl(8), *Inorg. Chem.*, 2017, **56**(6), 3483–3488.

22 P. Giannozzi, *et al.*, QUANTUM ESPRESSO: a modular and open-source software project for quantum simulations of materials, *J. Phys.: Condens. Matter*, 2009, **21**(39), 395502.

23 D. R. Hamann, Optimized norm-conserving Vanderbilt pseudopotentials, *Phys. Rev. B: Condens. Matter Mater. Phys.*, 2013, **88**, 085117.

24 D. R. Hamann, Erratum: Optimized norm-conserving Vanderbilt pseudopotentials [Phys. Rev. B 88, 085117 (2013)], *Phys. Rev. B*, 2017, **95**, 239906.

25 J. P. Perdew, K. Burke and M. Ernzerhof, Generalized Gradient Approximation Made Simple, *Phys. Rev. Lett.*, 1996, **77**(18), 3865–3868.

26 J. P. Perdew, K. Burke and M. Ernzerhof, Generalized Gradient Approximation Made Simple [Phys. Rev. Lett. 77, 3865 (1996)], *Phys. Rev. Lett.*, 1997, **78**(7), 1396–1396.

27 S. Grimme, Semiempirical GGA-type density functional constructed with a long-range dispersion correction, *J. Comput. Chem.*, 2006, **27**(15), 1787–1799.

28 E. Şaşıoğlu, C. Friedrich and S. Blügel, Effective Coulomb interaction in transition metals from constrained random-phase approximation, *Phys. Rev. B: Condens. Matter Mater. Phys.*, 2011, **83**, 121101(R).

29 A. Jain, *et al.*, Commentary: The Materials Project: A materials genome approach to accelerating materials innovation, *APL Mater.*, 2013, **1**, 011002.

30 E. Bianco, *et al.*, Stable Continuously Variable Temperature Cryo-STEM to Understand the Structurally Driven Phase Transition in the 2D Layered Magnet Nb3Br8, *Microsc. Microanal.*, 2020, **26**(S2), 1090–1092.

31 K. Godin, C. Cupo and E. H. Yang, Reduction in Step Height Variation and Correcting Contrast Inversion in Dynamic AFM of WS(2) Monolayers, *Sci. Rep.*, 2017, **7**(1), 17798.

32 C. J. Shearer, *et al.*, Accurate thickness measurement of graphene, *Nanotechnology*, 2016, **27**(12), 125704.

33 M. Navarro-Rodriguez, A. M. Somoza and E. Palacios-Lidon, Exploring surface charge dynamics: implications for AFM height measurements in 2D materials, *Beilstein J. Nanotechnol.*, 2024, **15**, 767–780.

34 M. I. Aroyo, *et al.*, Bilbao Crystallographic Server. II. Representations of crystallographic point groups and space groups, *Acta Crystallogr., Sect. A: Found. Adv.*, 2006, **62**(Pt 2), 115–128.

35 M. I. Aroyo, *et al.*, Bilbao crystallographic server: I. Databases and crystallographic computing programs, *Z. Kristallogr.*, 2006, **221**(1), 15–27.

36 M. I. Aroyo, *et al.*, Crystallography online: Bilbao Crystallographic Server, *Bulg. Chem. Commun.*, 2011, **43**(2), 183–197.

37 L. Liang and V. Meunier, First-principles Raman spectra of MoS2, WS2 and their heterostructures, *Nanoscale*, 2014, **6**(10), 5394–5401.

38 A. A. Osipov, High-temperature Raman spectroscopy, *Pure Appl. Chem.*, 2019, **91**(11), 1749–1756.

39 Z. Lin, *et al.*, Thermal expansion coefficient of few-layer MoS(2) studied by temperature-dependent Raman spectroscopy, *Sci. Rep.*, 2021, **11**(1), 7037.

40 X. Huang, *et al.*, Quantitative Analysis of Temperature Dependence of Raman shift of monolayer WS2, *Sci. Rep.*, 2016, **6**, 32236.

41 S. Liu, *et al.*, Thickness-dependent Raman spectra, transport properties and infrared photoresponse of few-layer black phosphorus, *J. Mater. Chem. C*, 2015, **3**(42), 10974–10980.

42 Z. Sun, *et al.*, Layer-dependent Raman spectroscopy of ultrathin Ta2Pd3Te5, *Phys. Rev. Mater.*, 2023, **7**, 094004.

43 H. Li, *et al.*, From Bulk to Monolayer MoS2: Evolution of Raman Scattering, *Adv. Funct. Mater.*, 2012, **22**(7), 1385–1390.